Trace-element-rich brines in eclogitic veins: implications for fluid composition and transport during subduction

Pascal Philippot, Jane Selverstone

Trace-element-rich brines in eclogitic veins: implications for fluid composition and transport during subduction

Pascal Philippot * and Jane Selverstone

Department of Earth and Planetary Sciences, Harvard University, 20 Oxford Street, Cambridge MA 02138, USA

Abstract. Primary and pseudosecondary fluid inclusions occur in oscillatory- and sector-zoned omphacite in eclogitic veins from the Monviso ophiolitic complex in the Western Alps. The inclusions contain aqueous brines and daughter crystals of halite, sylvite, calcite, dolomite, albite, anhydrite and/or gypsum, barite, baddeleyite, rutile, sphene, Fe oxides, pyrite and monazite. This daughter mineral suite indicates high solubilites of Na, K, Ca, Mg, Fe, Zr, Ti, P, Ba, Ce, La, Th, and S species and provides direct evidence for transport of high-field-strength, large-ion-lithophile, and light-rare-earth elements as dissolved species during subduction. Fluid-inclusion heterogeneities preserved within and between adjacent grains in the veins, however, suggest that the scale of fluid equilibration was small. A crack-seal geometry in some of the veins implies that fluid release in pulses rather than steady flow controlled mineral deposition and growth in the veins. From these observations, we develop a model of fluid release and entrapment in which pulses of fluid are associated in time with increments of shear and tensile failure; the rate of fluid release and the reduction in porosity both depend on the rate of plastic flow. Vein fluids may initially be derived from decrepitation of early fluid inclusions in the host eclogites. Small-scale fluid heterogeneities implied by the fluid inclusions in the veins are best interpreted in terms of limited fluid flow, and hence limited metasomatism. We conclude that element recycling into the mantle wedge during subduction will depend at least as strongly on fluid transport mechanisms as on element solubilities in the fluid phase. At Monviso, despite evidence for high trace element solubilities in saline brines, the elements were not removed from the downgoing slab prior to reaching depths of ~ 40 km.

* *Present address:* Laboratoire de Pétrologie Métamorphique, URA 736, CNRS, Université Pierre et Marie Curie, T26, E3, 4 Place Jussieu, F-75252 Paris Cedex 05, France

Introduction

Understanding the behavior of fluids in subduction zones is of fundamental importance in modeling island-arc magma genesis and element recycling to the mantle. Recent studies (e.g., Perfit et al. 1980; Wyllie 1984, 1988; Arculus and Powell 1986; Tatsumi et al. 1986; Wilson 1989; Vidal et al. 1989) generally agree that magma generation in subduction zone environments involves variable contributions of the mantle wedge and a metasomatic component; the metasomatic component may be either a fluid or a partial melt derived from the subducted slab. Prograde metamorphic dehydration of the oceanic crust and associated sediments should release a substantial volume of fluid during subduction, as Peacock (1990) has shown through thermal modeling and flux calculations. Whether or not this fluid will ascend into the overlying mantle wedge or be retained as a grain boundary phase in the slab, however, will depend upon its wetting properties and the stress regime of the slab and wedge. The wetting properties in turn depend upon the compositions of both the fluid phase and its solid host (e.g., Watson and Brenan 1987; Yardley and Bottrell 1988).

At present there are few data bearing directly on the composition of the fluids accompanying high-pressure low-temperature (H*P*-L*T*) metamorphism. On the basis of mineral assemblages (e.g., Ernst 1972; Holland 1979) and isotopic studies (e.g., Taylor and Coleman 1968; Matthews and Schliestedt 1984) many authors have argued for an H_2O-rich fluid attending H*P*-L*T* metamorphism. This conclusion, however, is in striking contrast to the few available studies on fluid inclusions in eclogites and blueschists that show a wide range of CO_2, H_2O, N_2, CH_4, and saline fluids (Luckscheiter and Morteani 1980; Sobolev et al. 1986; Andersen et al. 1989; Franz et al. 1989; Klemd 1989; Selverstone et al. 1990; this study). As pointed out by Selverstone (1986), fluid heterogeneities and possible immiscibility may have

important implications for our understanding of subduction zone processes. Interaction of H*P*-L*T* rocks with fluids of different compositions may have a strong effect on: (1) mineral phase equilibria and, as a consequence, the rheological properties of the rocks; (2) metasomatic effects as a result of the different element solubilities in fluids of different composition; (3) heat transfer processes as a result of the different heat capacities of the fluids.

Thus, two factors of critical importance in controlling subduction zone processes are currently only poorly constrained: (1) the mechanisms and paths by which fluids escape toward the mantle wedge; (2) the nature of the fluid phase accompanying H*P*-L*T* metamorphism. The aims of this paper are to present evidence from primary fluid inclusions for the nature of fluids accompanying H*P*-L*T* metamorphism in the Monviso area and to develop a model of fluid migration by evaluating possible sources and conditions of fluid escape and entrapment in these eclogitic rocks.

Geologic setting

The rocks in this study are eclogites from the Monviso meta-ophiolitic complex in the French-Italian Western Alps (Fig. 1). This massif represents a vestige of the Neotethys basin that separated the South Alpine plate from the European plate during Cretaceous time (e.g. Elter 1971), and that closed by progressive subduction during late Cretaceous through Eocene time (e.g., Dal Piaz 1974; Ernst and Dal Piaz 1978). Previous petrologic studies show that the area equilibrated successively under eclogite, blueschist and greenschist facies conditions (e.g., Lombardo et al. 1978), although none of the samples in this study show evidence for overprinting during uplift.

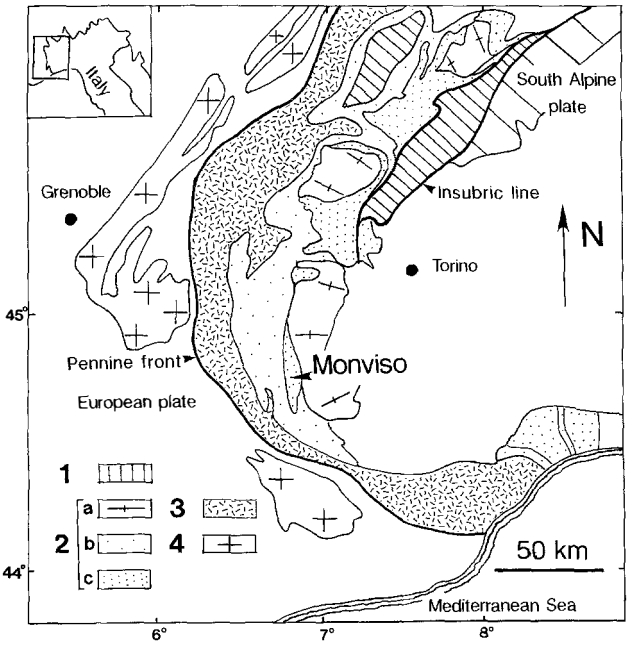

Fig. 1. Schematic map of the Western Alps showing location of the Monviso complex. *1* Austro-Alpine nappes; *2* Internal Pennine Zone, *a* Internal Crystalline Massifs, *b* schistes lustrés, *c* main ophiolite complexes; *3* External Pennine Zone (i.e. Briançonnais Zone); *4* External Crystalline Massifs

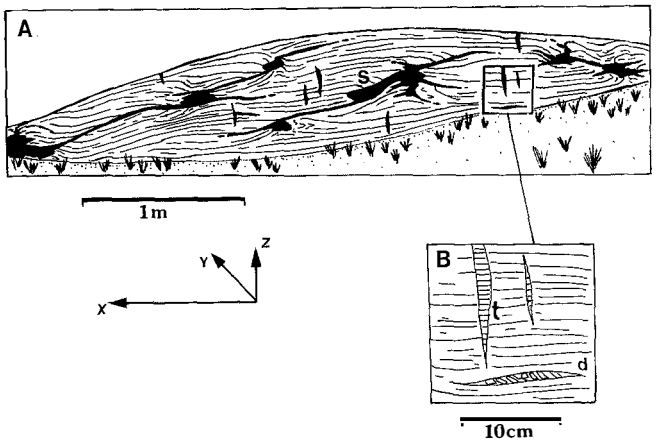

Fig. 2. Sketch of a foliation boudin of eclogitic metagabbro from the Lago Superiore region showing the geometry of the three vein types with respect to the finite strain markers; *s*=shear fracture, *t*=tension gash, *d*=dilatant fracture

In the Monviso complex, unaltered eclogitic rocks are preserved in Fe-rich metagabbros from the Lago Superiore cumulate sequence (e.g., see Lombardo et al. 1978 and Philippot 1988 for location). The Fe-rich metagabbros occur near the top of the sequence in association with Mg-rich metagabbros and talc schist layers. The main structure in the sequence is a 10- to 30 m-thick major ductile shear zone composed of highly-deformed mylonitic rocks and bounded above by a thrust fault (Philippot and Kienast 1989). The shear zone is defined by 10×1 m oliation boudins (e.g., Platt and Vissers 1980) outlining a complex interference pattern of folds in the metagabbros and talc schists. Veining comprises an important element of the structure (Philippot 1987). The boudins of Fe-rich metagabbroic eclogite display three types of eclogitic veins (Fig. 2): (1) *tension gashes* that trend subperpendicular to the foliation plane and the stretching lineation; (2) *dilatant fractures* that are parallel to the foliation plane; (3) complex sets of *shear fractures* that randomly crosscut the foliation plane and the stretching lineation. These latter may partly or totally represent foliation boudinage veins. *Tension gashes* and *dilatant fractures* are small (centimeter wide by 20–50 cm long) in comparison with dm to m-scale *shear fractures*. Boudins, folds and fractures are thought to have formed progressively during non-coaxial deformation (see Philippot 1987, 1988 and Philippot and Kienast 1989 for details).

In the Lago Superiore region, temperatures of the eclogitic metamorphism have been estimated at $450 \leq T \leq 550°$ C by several authors (Lombardo et al. 1978; Kienast 1983; Lardeaux et al. 1986). Philippot and Kienast (1989), however, showed that garnet-pyroxene pairs yield inconsistent results because of the strong dependence of calculated T on the amount of Fe^{3+} in the pyroxene, and possibly on non-ideal substitution between omphacite and acmite. Despite the absence of an accurate method for estimating temperatures in iron-rich eclogitic metagabbros, we consider $500 \pm 50°$ C to be a reasonable T range for eclogite facies metamorphism in the Lago Superiore region. All authors agree on minimum pressure conditions of 10–11 kbar.

Mineralogy and microtextures

In general, the *mylonitic rocks* and the *shear fractures* contain the same mineral assemblage: omphacite + garnet + rutile + apatite; within the fractures, garnet, rutile, and apatite occur in randomly distributed millimeter- to centimeter-scale clusters, whereas they are more evenly distributed in the host mylonite. *Tension gashes* and *dilatant fractures* lack garnet but may contain a small amount of rutile or apatite. Small, interstitial crystals of albite occur locally between omphacite grains in all three types of veins. A detailed

textural analysis of the mylonitic rocks and the veins is given in Philippot (1987) and Philippot and Kienast (1989) and only a brief review is included here.

Mylonites

In the mylonitic rocks, moderately and highly strained layers (1–10 cm thick) alternate parallel to the foliation plane. The moderately strained layers contain pyroxene porphyroclasts (10–30 vol.% of the rocks) in association with a fine-grained matrix composed of recrysatllized pyroxene, fractured rutile and inclusion-rich garnet (0.2–0.5 mm). The pyroxene porphyroclasts (2–5 mm) are strained (undulose extinction) and show development of subgrain boundaries. From TEM studies, Lardeaux et al. (1986) suggested that plastic deformation of pyroxene resulted in strain-free subgrain development at the expense of strained porphyroclasts by progressive rotation of the subgrain boundaries. In the more highly strained layers dynamic recrystallisation of porphyroclasts down to a grain size of 10 µm produced a marked preferred orientation within the foliation plane. Locally, however, static recrystallization of pyroxene has resulted in a mosaic texture characterized by blocky and randomly oriented grains. Associated garnets are equigranular (0.1–0.2 mm in diameter), subhedral, and frequently atoll-shaped (see Fig. 11).

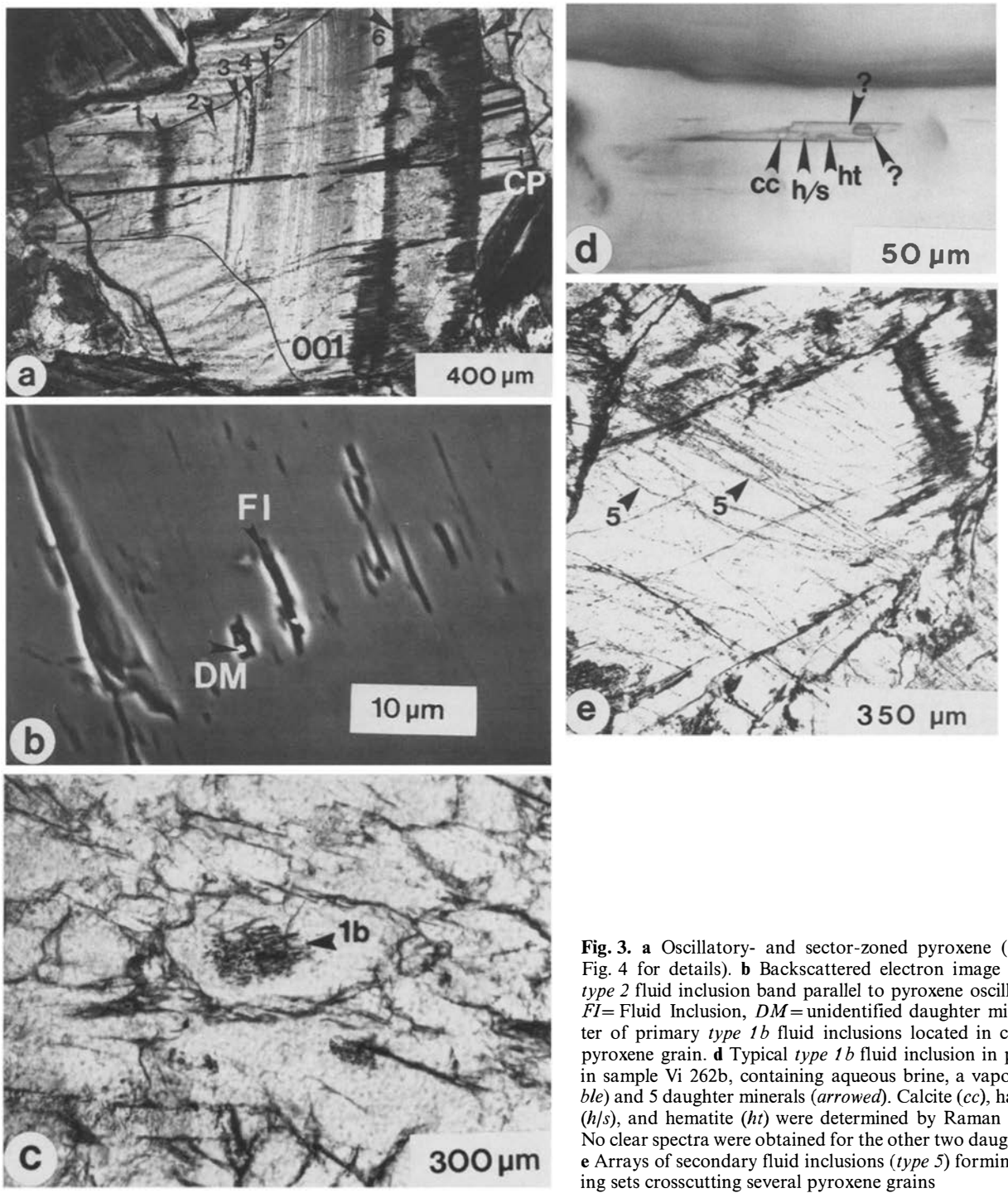

Fig. 3. **a** Oscillatory- and sector-zoned pyroxene (see sketch in Fig. 4 for details). **b** Backscattered electron image of a primary *type 2* fluid inclusion band parallel to pyroxene oscillatory zoning. *FI*= Fluid Inclusion, *DM*= unidentified daughter mineral. **c** Cluster of primary *type 1b* fluid inclusions located in core of a vein pyroxene grain. **d** Typical *type 1b* fluid inclusion in pyroxene core in sample Vi 262b, containing aqueous brine, a vapor phase (*bubble*) and 5 daughter minerals (*arrowed*). Calcite (*cc*), halite or sylvite (*h/s*), and hematite (*ht*) were determined by Raman spectroscopy. No clear spectra were obtained for the other two daughter minerals. **e** Arrays of secondary fluid inclusions (*type 5*) forming anastomosing sets crosscutting several pyroxene grains

Eclogitic veins

Within the *dilatant veins* and *shear fractures*, many of the pyroxene grains show spectacular oscillatory and sector zoning. These features are particularly well represented in sample Vi385, in which pyroxene occurs in association with small, interstitial albite grains. The pyroxene grains range between 0.2 and 4.5 mm in length, with an average around 1–2 mm. In thin section, a typical crystal consists of two zones (Figs. 3a, 4): (1) a small, optically unzoned core; (2) an oscillatory zoned subhedral to euhedral mantle. The (001) growth zones (i.e. basal faces) are generally 2 to 5 times thicker than the prismatic faces. The oscillatory zones consist of sharply demarcated bands of irregular width (10–40 μm in the basal face, 2–10 μm in the prismatic face). The bands are generally continuous from one face to another, implying variations in thickness of the concentric zones across the growth-sector boundaries. In some crystals, the bands forming the basal faces are offset across fractures oriented normal to the zonation.

Detailed microprobe traverses were performed normal to the basal face in four adjacent oscillatory-zoned pyroxene crystals from a single vein (sample Vi 385; *dilatant* or *shear fracture*). Mineral compositions were determined with a Camebax electron microprobe in the Department of Earth and Planetary Sciences at Harvard University, operating at 20 kV accelerating voltage, 15 nA beam current with a beam-spot diameter of ~1 μm. Analyses were performed at 10 μm intervals along a line perpendicular to the basal face. In all analyzed grains, the boundaries of the concentric zones were normal to the surface of the thin section, thus avoiding averaging of adjacent concentric zones. Representative profiles from two adjacent grains are shown in Fig. 5 (the location of profile [b] is shown in Fig. 3a and 4), in which values for Ca and Na in the M2 site are plotted against the distance from core to rim. Contents of Ca and Na are associated with diopside and jadeite contents in omphacite, respectively. All four analyzed grains show relatively jadeite-rich cores and diopside-rich rims, but there is no correlation in the fine-scale zoning patterns between grains, as is evident in the profiles for two adjacent grains shown in Fig. 5.

Within the *tension gashes*, many of the pyroxene grains are fibrous and are oriented with their long axes parallel to the stretching direction of the host country rocks. These pyroxene grains are thought to have grown during successive crack-seal increments, as described in detail by Philippot (1987).

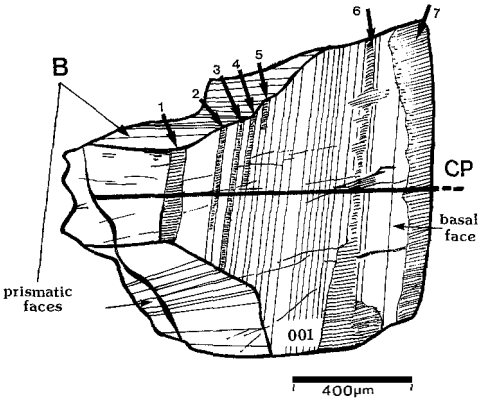

Fig. 4. Sketch of the oscillatory-zoned pyroxene in Fig. 3a showing a well-developed basal (001) face and narrower prismatic faces. The line normal to the basal face (*CP*) shows location of chemical profile in Fig. 5b. *Arrows* indicate bands of *type 2* fluid inclusions parallel to concentric growth zones. Note the presence of two discontinuous inclusion bands (band nos. 4 and 5 not included in the profile). Distribution of the daughter minerals varies from one fluid inclusion band to another. Identified daughter minerals are: band *1* = calcite, baddelleyite, monazite; band *2* = dolomite; band *3* = gypsum and/or anhydrite, albite, baddelleyte, pyrite?; band *4* = barite, calcite; band *6* = monazite; band *7* = halite, sylvite, calcite

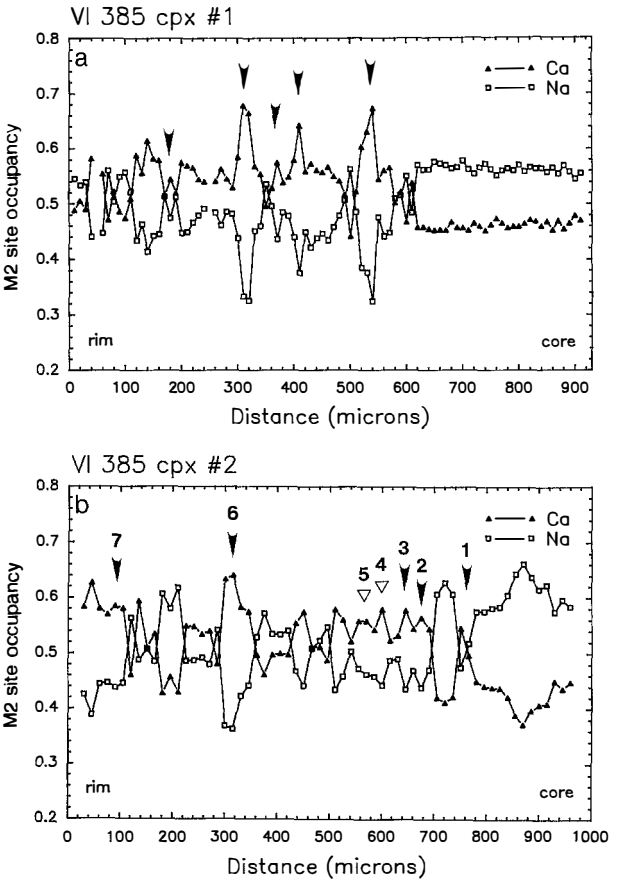

Fig. 5a, b. Chemical-zoning profiles normal to the basal faces of two adjacent pyroxene grains; **b** profile shown in Figs. 3a, 4 as "CP". Variations in Ca and Na in M2 site (i.e., diopside and jadeite contents in omphacite, respectively) are plotted vs distance core–rim. *Black arrows* point to the location of fluid-inclusion bands parallel to the concentric growth zones. *Open arrows* in profile **b** point to the location of two discontinuous fluid inclusion bands in Figs. 3a, 4 not included into the profile

Fluid inclusion occurrence

Five different textural types of fluid inclusions were found in the Monviso mylonites and associated eclogitic veins: *type 1* inclusions occur as evenly distributed clusters in the cores of pyroxenes in both the mylonites (*type 1a*) and veins (*type 1b*); *type 2* inclusions line the oscillatory growth zones of pyroxenes in the *dilatant veins* and *shear fractures; type 3* inclusions occur along crack-seal microcracks within individual pyroxene and possibly rutile grains; *type 4* inclusions are irregularly shaped inclusions clearly formed by necking down of earlier inclusions in vein garnet; *type 5* inclusions occur along healed fractures that crosscut grain-boundaries. *Type 5* inclusions are clearly secondary in origin; these inclusions were too small to analyze (< 5 μm) and are not discussed further in this study. Detailed descriptions of the remaining inclusion types are given below.

Type 1

Within the mylonites, clusters of 5–30 μm tubular and irregular fluid inclusions (*type 1a*) occur in the cores

of relic pyroxene porphyroclasts, whereas recrystallized strain-free omphacites generally do not contain fluid inclusions. Clusters of fluid inclusions (*type 1b*) also occur within the cores of massive and randomly oriented pyroxene blasts (millimeters–centimeters insize) in all vein types (Fig. 3c). These fluid inclusions show generally irregular shapes and a wide range in sizes (1–60 μm). Locally, the presence of star-shaped inclusions indicates that some of the inclusions partially decrepitated, and hence that their densities may have been modified after entrapment. *Type 1b* inclusion clusters are also found in apatite from shear fractures; these inclusions are round to irregular and range in size from a few microns to several tens of microns. In interstitial albite in all vein types, fluid inclusions are either isolated or form small clusters of 2 to 3 inclusions of irregular shape and variable size (5–30 μm); these are also thought to be *type 1b* inclusions. The restriction of *type 1a* and *type 1b* inclusions to the cores of grains and the absence of *type 1a* inclusions from recrystallized pyroxene in the mylonites suggests initial entrapment as primary inclusions.

Type 2

Two- to 50 μm-wide bands of fluid inclusions decorate concentric zones on (001) faces of oscillatory-zoned vein pyroxenes (Fig. 3a, b) and provide convincing textural evidence for entrapment as primary inclusions during pyroxene growth in the *dilatant veins* and *shear fractures*. The fluid inclusion bands may be continuous or discontinuous within a single concentric zone, generally end abruptly at growth sector boundaries, and are typically offset across fractures. Individual inclusions are tubular, 2–30 μm long and 1–5 μm wide, with an average size of 15×2 μm; their long axes are invariably oriented normal to the (001) growth zones. Rare and discontinuous fluid inclusion bands have also been observed decorating growth zones on the prismatic faces of the same pyroxene hosts. Locations of several fluid inclusion bands are shown by the arrows in Figs. 3–5. There is no correlation in the location of fluid inclusion bands between adjacent grains (Fig. 5), just as there is no correlation in the chemical zoning profiles of adjacent pyroxenes. In all grains, however, the fluid inclusion bands are confined to diopside-rich zones, implying a possible connection between development of the oscillatory zoning and the fluid phase.

Type 3

In some *tension gashes*, fluid inclusions occur in healed microcracks oriented at a high angle to the long axes of fibrous pyroxenes that crosscut the veins from wall to wall. These cracks are interpreted to have formed during the progressive opening of the veins (i.e., growth by a crack-seal mechanism; Philippot 1987), and thus may have entrapped nearly primary fluids. Individual fluid inclusions within the cracks are either tubular (10–40 μm long and a few microns across) with their long axis parallel to the long axis of the fibers (i.e., [001] direction) or show round to irregular shapes 1–10 μm in diameter; the trails of inclusions do not cross grain boundaries, suggesting that the inclusions are pseudosecondary based on the textural criteria of Roedder (1984). In rutile from *shear fractures,* small ($\leq$10 μm) round to elliptical fluid inclusions occur in bands oriented parallel to one another within any one grain. The inclusion bands form small segments of different length that do not cross grain boundaries. Although it remains impossible to establish a relationship between the orientation of the bands, the grain morphology and the vein structure, the geometry of the fluid inclusion bands is similar to the healed microcracks found in the fibrous pyroxenes described above, suggesting that these inclusions may also have been trapped during grain growth in a crack-seal vein environment.

Type 4

In garnet from *shear fractures*, fluid inclusions occur in randomly oriented planes that never crosscut an entire grain. The inclusions are flat, show irregular shapes, and a wide range of sizes (1–40 μm). This range of inclusion sizes and their very irregular shape suggest that considerable recrystallization and necking down of large inclusions have formed multiple smaller inclusions. There is no clear evidence for the timing of entrapment of *type 4* inclusions, but the fact that the arrays of *type 4* inclusions do not cross grain boundaries suggests that they also may be pseudosecondary (e.g., see Fig. 3–14 in Roedder 1984) in origin.

Several textural features, in addition to those described for *type 4* inclusions, indicate that many of the fluid inclusions have undergone some recrystallization and necking down. In pyroxene, daughter minerals in some instances are partly entrapped in the host wall. Extended recrystallization of the host is particularly clear in some apatite grains in which a coat on the wall or "bridge" between two inclusions is optically visible. Within any one population, however, the inclusions show fairly consistent phase ratios and yield similar temperatures of homogenization (see below), suggesting that any post-entrapment modification was largely completed before the nucleation of additional phases (solid or vapor) occurred.

Fluid inclusion analyses

The fluid inclusions from seven samples (Vi 258: omphacite (omp)+garnet (gar)+rutile (rt)+apatite (ap); Vi 260: omp+ap+interstitial albite (ab); Vi 262b: omp+rat+ap; Vi 263: omp+gar; Vi 378: omp+ap; Vi 385: omp+ab; and Vi 389: omp+rt+ab; Figs. 6, 7 and Table 1) were analyzed by a combination of microthermometry, laser Raman microspectrometry and electron microprobe techniques; the results of each of these techniques are summarized below. At room temperature, all inclusions contain a liquid phase, a vapor phase, and

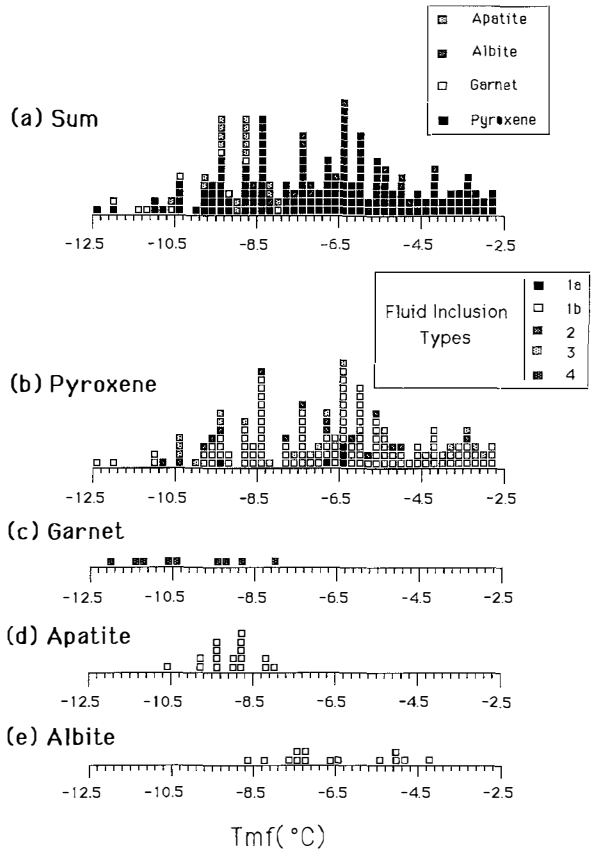

Fig. 6. Final melting temperatures (*T*mf) of primary and pseudosecondary fluid inclusions

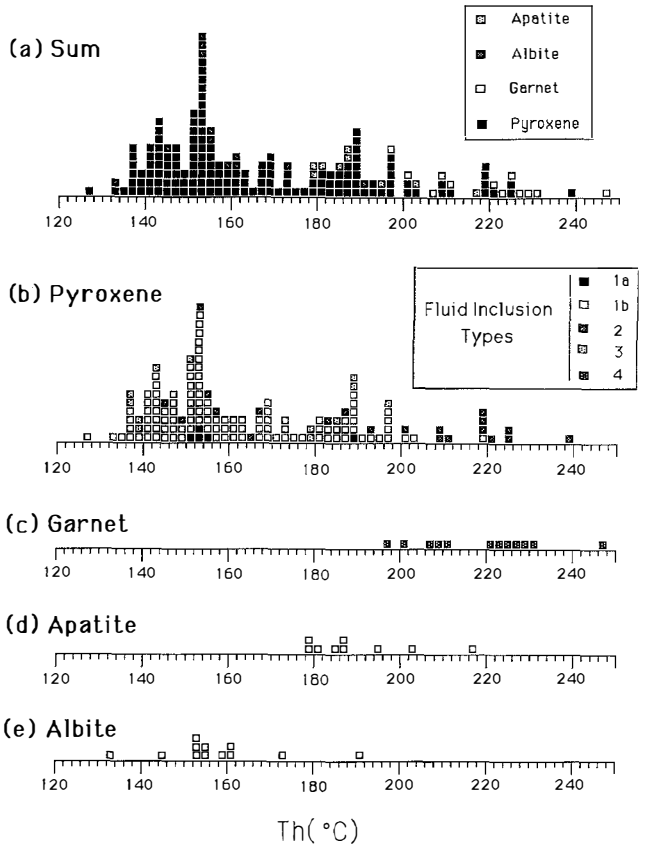

Fig. 7. Homogenization temperatures (*T*h) of primary and pseudosecondary fluid inclusions

up to 5 daughter minerals (Fig. 3 d; Table 1). The volume percent vapor phase estimated by visual inspection of the fluid inclusions (e.g., Roedder 1984, p. 103) ranges between 0.1 and 2.0%. None of the daughter phases except rutile was observed as isolated solid inclusions in any of the host minerals, and the daughter crystals generally show uniform phase ratios with respect to the size of the fluid inclusions; both of these facts imply that the solids are "valid" daughter minerals that precipitated during cooling and therefore are not accidentally trapped solids (e.g., Roedder 1984, pp 53–55).

Microthermometry

Microthermometric measurements were made with a modified U.S. Geological Survey freezing-heating stage with nitrogen as the cooling medium. The temperatures of final melting (*T*mf) and of homogenization (*T*h) were determined at heating rates of $\sim 0.1\,^{\circ}C\ min^{-1}$ and $\sim 1.0\,^{\circ}C\ min^{-1}$, respectively. *T*mf and *T*h measurements were reproducible to $\pm 0.1\,^{\circ}C$ and $\pm 1.0\,^{\circ}C$, respectively. Most of the microthermometric data presented below were obtained in pyroxene (161 measurements out of 204: 5 in *type 1a*, 120 in *type 1b*, 21 in *type 2*, 15 in *type 3* fluid inclusions; Table 1; Figs. 6, 7). Only a few analyses were performed in vein garnet (12), apatite (17), and albite (14).

All inclusions, both in the mylonitic rocks and in the veins, show consistent behavior at low and high temperatures. On the warming of frozen inclusions, visible melting of ice and/or hydrates starts between -24.5 and $-20\,^{\circ}C$ and ends (*T*mf) between -12.5 and $-2.9\,^{\circ}C$ in pyroxene, -12 and $-8.0\,^{\circ}C$ in garnet, -10.7 and $-8.0\,^{\circ}C$ in apatite and -8.6 and $-4.3\,^{\circ}C$ in albite (Fig. 6, Table 1). Melting and homogenization phenomena were difficult to observe in rutile (due to color of the grains), and thus no data for rutile are presented here. Note that *T*mf for albite is substantially higher than for apatite and garnet. However, the range of pyroxene *T*mf overlaps the range for garnet, apatite and albite, suggesting that the differences observed between albite and garnet + apatite may be an artifact of the few data available. The melting solid generally forms a fine-grained aggregate that recrystallizes into several coarser grains during heating; it cannot be identified with certainty, however, and could be ice or a salt hydrate, or both. As described below, distribution of the daughter crystals in the inclusions is heterogeneous and varies from grain to grain, suggesting that both ice and hydrates of a variety of salts (e.g., NaCl, KCl, $\pm CaCl_2 \pm MgCl_2 \pm FeCl_2$?) in various proportions may be present in different inclusions, which in turn may affect the melting behavior of the fluids.

On heating, the liquid + vapor phases in the inclusions homogenize to liquid (*T*h) 113–240 °C in pyroxene

Table 1. Summary of fluid inclusion data

Sample	Host rock	Host mineral	FI type[a]	Geometry	Size range (μm)	No. analyzes	*T*mf range (°C)	*T*h range (°C)	Wt% Eq. NaCl	Daughter minerals
Vi 258	Shear fracture	Pyroxene	1b	Irregular	5 × 15/11 × 30	12	−2.9/−6.3	138/181	[b]	Calcite, halite, sylvite, pyrite
		Garnet	4	Flat, irregular	8 × 28/12 × 32	2	−8.0/−8.8	198/200	[b]	Too small to determine
Vi 260	Mylonite	Pyroxene	1a	Irregular, tubular	1 × 20/3 × 44	4	−6.4/−9.3	153/165	[b]	Calcite, halite, sylvite, pyrite
	Shear fracture	Pyroxene	1b	Irregular, tubular	1 × 4/38 × 67	33	−3.4/−12.5	113/167	[b]	Calcite, halite, sylvite, pyrite, hematite, sphene
		Albite	1b	Irregular	2 × 9/19 × 39	9	−5.1/−8.6	145/192	[b]	Halite, calcite?
Vi 262b	Tension gash	Pyroxene	1b	Irregular, tubular	2 × 10/14 × 52	18	−2.9/−11.0	126/201	[b]	Calcite, halite, sylvite, pyrite
			3	Elliptical	3 × 6/4 × 44	15	−3.0/−10.5	134/208	[b]	Calcite, halite, sylvite, pyrite, hematite, rutile
Vi 263	Shear fracture	Pyroxene	1b	Irregular	5 × 5/11 × 43	15	−3.3/−9.8	168/211	[b]	Calcite, halite, sylvite, pyrite
		Garnet	4	Flat, irregular	2 × 4/22 × 27	10	−9.2/−12.0	206/248	[b]	Halite, pyrite, calcite?, sylvite?
Vi 378	Shear fracture	Pyroxene	1b	Irregular	1 × 1/6 × 30	22	−5.5/−9.9	140/197	[b]	Calcite, halite, sylvite, pyrite
			2	Tubular	2 × 6/4 × 52	10	−5.1/−7.8	145/167	[b]	Halite, sylvite, hematite, calcite?
		Apatite	1b	Irregular	3 × 8/16 × 32	17	−8.0/−10.7	179/217	[b]	Halite, hematite, pyrite, sylvite?, calcite?
Vi 385	Dilatant vein or shear fracture	Pyrexone	2	Tubular	1 × 10/3 × 26	11	−3.4/−10.7	170/240	5.5/14.7	Calcite, halite, sylvite, pyrite, Fe oxide, rutile, dolomite, albite gypsum/anhydrite, baddeleyite, barite, monazite (see text and Fig. 4)
Vi 389	Mylonite	Pyroxene	1a	Tubular	2 × 25	1	−6.5	190	[b]	Halite, pyrite, sylvite?
	Shear fracture	Pyroxene	1b	Irregular, tubular	4 × 18/6 × 38	20	−2.9/−8.8	138/194	[b]	Halite, sylvite, calcite, pyrite, rutile, gypsum/anhydrite
		Albite	1b	Irregular	7 × 9/10 × 12	5	−4.3/−7.5	132/172	[b]	Halite, pyrite, sylvite?

[a] Fluid inclusion type: 1a, cluster in core of mylonite pyroxene; 1b, cluster in core of vein pyroxene, apatite, albite; 2, on growth band in oscillatory-zoned vein pyroxene; 3, on crack-seal microcracks; 4, small inclusions formed by necking down of large flat inclusions (vein garnet only)

[b] Salinities determined only for type 2 inclusions lacking halite and sylvite daughters; see text for discussion

(peak at ~150 °C), 198–248 °C in garnet, 179–217 °C in apatite, and 132–192 °C in albite (Fig. 7; Table 1). In garnet, *T*hs are scattered and do not show a clear peak. Temperatures of homogenization for garnet and apatite are generally higher than the average *T*h for pyroxene and albite; this may, however, be an artifact due to the few available data for garnet, apatite and albite. Further heating up to 500 °C led to decripitation of the fluid inclusions before dissolution of any of the daughter minerals could be observed.

Identification of daughter minerals

Identification of the solid phases in the inclusions was performed in-situ by direct analyses with: (1) the electron microprobe in the Department of Earth an Planetary Sciences, Harvard University; (2) and Instruments S.A. U1000 Raman microprobe equipped with a monochannel photomultiplier tube in the Department of Geological Sciences, Virginia Polytechnic Institute and State University of Blacksburg, USA; (3) a Dilor Microdil 28 multichannel Raman microprobe in the Département de Pétrologie et de Minéralogie de l'Université des Sciences et Techniques de Nantes, France. Electron-microprobe analyses were carried out in inclusions in pyroxene in samples Vi 262b (*type 1b* and *3* inclusions), Vi 385 (*type 2* inclusions), and Vi 389 (*type 1b* inclusions); Raman analyses were carried out in *type 1b* fluid inclusions in pyroxene, apatite and albite in all samples except Vi 385, in *type 2* fluid inclusions in sample Vi 378 (the *type 2* daughter minerals in sample Vi 385 were too small to be analysed by Raman techniques), and in *type 3* fluid inclusions in sample Vi 262b. In garnet, *type 4* daughter minerals were identified by comparing morphologies and differences in refractive index of the daughters with daughter crystals identified in other hosts.

Electron microprobe analyses of the daughter minerals were made in open fluid inclusions located at the surface of the thin sections (Fig. 3b). Daughter crystals identified by this technique include; calcite, dolomite, albite, anhydrite and/or gypsum, barite, baddeleyite, rutile, Fe oxide, halite, sylvite, pyrite and monazite (Table 1). Specifically, *type 1b* and *type 3* inclusions contain halite + sylvite + pyrite ± calcite ± rutile ± Fe oxide ± gypsum/anhydrite. *Type 2* inclusions contain daughter mineral assemblages that vary dramatically from one pyroxene growth zone to the next; within a single grain the following daughter assemblages were identified: (1) calcite + baddeleyite + monazite; (2) dolomite; (3) gypsum/anhydrite + albite + baddeleyite ± pyrite; (4) barite + calcite; (6) monazite; (7) halite + sylvite + calcite (see Figs. 3, 4 for locations of these inclusion bands). Unfortunately, owing to the small size of the *type 2* inclusions, it was impossible to correlate accurately the daughter mineral suites identified by microprobe with the microthermometric data obtained from adjacent fluid inclusion chips.

Raman microprobe analysis of daughter minerals in omphacite is made difficult by interference of several

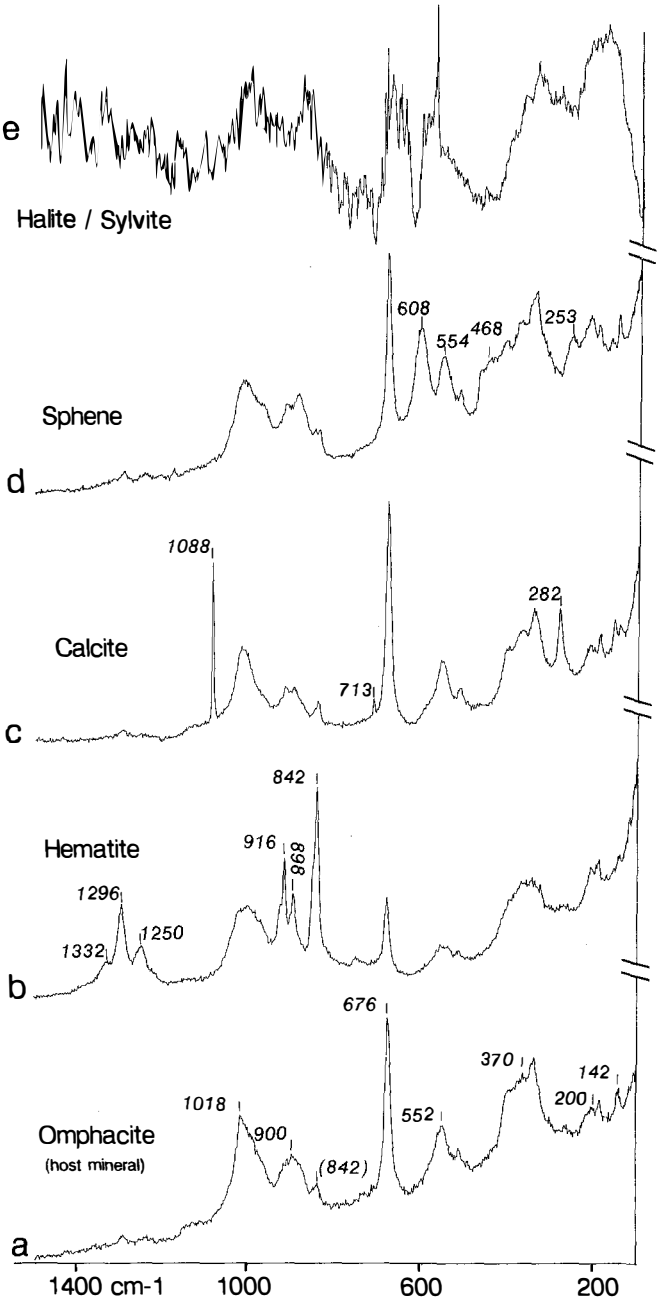

Fig. 8a–e. Raman spectra of the daughter minerals in primary fluid inclusions in vein pyroxene (spectra obtained at VPI). **a** Omphacite host-mineral spectrum with peaks at 142, 200, 370, 552, 676, 842 (microscope-lens peak), 900 and 1,018 cm^{-1}. **b, c, d** and **e** examples of daughter mineral spectra overlapping the omphacite spectrum shown in **a** for comparison. **b** Hematite spectrum with peaks at 842, 898, 916, 1,250, 1,296 and 1,332 cm^{-1}. **c** Calcite spectrum with peaks at 282, 713 and 1,088 cm^{-1}. **d** Sphene spectrum with peaks at 253, 468, 554 and 608 cm^{-1}. **e** Noisy spectrum of large rectangular solid phase indicating halite or sylvite

peaks of the host pyroxene at 142, 200, 370, 552, 676, 900 and 1,018 cm^{-1} (Fig. 8a). In addition, the spectra in Fig. 8a show a small peak at 842 cm^{-1} that characterizes the lens of the microscope (C.J. Knight, personal communication). Despite these difficulties, however, hematite, calcite, rutile, and sphene were confirmed by Raman analysis (Fig. 8), and halite, sylvite, and pyrite in-

ferred. The latter three minerals do not show clear Raman spectra, but noisy spectra (Fig. 8e) obtained on large, colorless, rectangular daughters and smaller, square, opaque daughters are consistent with identities of halite/sylvite and pyrite, respectively. Anhydrite and/or gypsum were not found with Raman, possibly because of overlap between the Ca-sulfate peak at 1,017 cm^{-1} and a marked peak in the host omphacite spectrum at 1,018 cm^{-1} (Fig. 8a). The identified daughter mineral suites are summarized by inclusion type in Table 1.

Fluid inclusion compositions

The microthermometric analyses coupled with identification of the daughter phases imply that the fluids filling the eclogitic minerals are complex aqueous brines containing varying amounts of Na, K, Ca, Mg, Fe, Si, Al, Zr, Ti, P, Ba, Ce, La, S, CO_3^{-2}, and Cl species. Despite the presence of carbonate, sulfate, and sulfide daughter minerals in many inclusions, neither CO_2 nor any sulfur species were detectable by microthermometric or Raman techniques on the liquid and vapor phases. There is also no evidence for N_2 or CH_4 in any of the inclusions. The daughter mineral assemblages listed in Table 1 do, however, suggest variations in oxygen and sulfur fugacities (f_{O_2} and f_{S_2}) between different inclusion populations.

The microthermometric data for *type 1* and *type 3* inclusions present some apparent inconsistencies that make determination of specific inclusion compositions difficult. Nearly all of these inclusions contain daughter crystals of halite and sylvite, indicating that the fluids are saturated with respect to NaCl and KCl; observed initial melting below -22.9 °C (eutectic temperature in the system $NaCl-KCl-H_2O$) in some of the inclusions points to the presence of additional components in the fluid, consistent with the presence of Ca- and Fe-bearing daughter mineral phases, (e.g., calcite, pyrite). Under equilibrium conditions in the $NaCl-H_2O$ system, and NaCl-saturated inclusion (26.3–61.9 wt% NaCl) should form a hydrate, $NaCl \cdot 2H_2O$, during cooling that melts incongruently to NaCl + solution at 0.1 °C during subsequent heating. Clearly, the recorded values of Tmf ≤ -2.5 °C are inconsistent with this expected behavior, and at first glance are more suggestive of low- to moderate-salinity inclusions. However, addition of KCl to the system lowers the peritectic temperature from $+0.1$ to -2.3 °C (e.g., Roedder 1984), which is in agreement with our highest-recorded values of Tmf but not the lower values. Addition of other species, such as $CaCl_2$, $FeCl_2$, etc., to the system will affect both the melting behavior of the inclusions (e.g., Williams-Jones and Samson 1990) and the solubilities of NaCl and KCl. As summarized by Roedder (1984), addition of Ca or Mg to the system greatly reduces the solubility of NaCl, such that daughter crystals of NaCl can be present in inclusions containing only a few percent NaCl rather than >26 wt%. The difficulties of observing the first melting and identifying the hydrate species, means that we are not able to determine with certainty either the specific brine system represented by *type 1* and *type 3* inclusions or their total salinities. The daughter-mineral suite, however, indicates that the inclusions contain brines in the system $H_2O-NaCl-KCl \pm CaCl_2 \pm FeCl_2$, in addition to S and CO_2 (which were not detectable by Raman).

Approximate salinities can be estimated from *type 2* inclusions, which typically lack halite and sylvite daughter phases (see above and Fig. 4). Values of Tmf in these inclusions indicate salinities of ~5–15 wt% NaCl equivalent (Table 1). These estimated salinities are subject to large uncertainties, however, as the daughter mineral suite indicates the presence of varying amounts of Ca, Fe, Mg, Zr, Ti, Na, Si, Al, Ba, Ce, La, CO_2, and S species in these inclusions; the effects of these additional components on salinity calculations is unknown, and we used the 5–15% equivalent NaCl values with caution.

Fluid inclusion densities

A major problem that arises when studying fluid inclusions that have undergone HP-LT metamorphism and rapid uplift to the surface is that the P–T conditions inferred from the fluid inclusions do not agree with those inferred from mineral thermobarometry (e.g., Klemd 1989). On the basis of experimental studies in the system $H_2O-NaCl$, Sterner and Bodnar (1989) showed that densities of fluid inclusions formed during early stages of regional metamorphism probably reequilibrate during burial and subsequent uplift in response to differential pressure, although inclusion compositions are likely to be preserved. The textural evidence that many of the Monviso inclusions are primary and were entrapped during eclogitic vein formation implies that compositions of the inclusions can provide direct evidence for the nature of the fluids accompanying subduction zone metamorphism, although processes such as necking down and/or partial decrepitation undoubtedly modified the densities of many inclusions.

Estimating densities of most of the inclusions is difficult owing to: (1) the wide variety of daughter crystals, implying that different inclusions have very different compositions that cannot be accurately determined; (2) the generally irregular shapes of the inclusions that preclude accurate determination of inclusion and daughter mineral volumes. As a result, densities and hence isochores for most inclusions have not been determined. We have, however, determined model densities and isochores for the *type 2* inclusions from sample Vi 385 for which we were able to estimate salinities (isochores calculated from the data of Zhang and Frantz 1987, assuming the inclusion fluids are in the system $H_2O-NaCl$). As can be seen from Fig. 9, the isochores underestimate the eclogite P–T conditions by at least 5 kbar. These isochores can only be considered approximations, however, owing to the fact that the inclusions contain daughter crystals of calcite ± dolomite ± barite ± baddeleyite ± monazite ± Fe oxide ± rutile ± gypsum/anhydrite ± albite; it was not possible to estimate the effect that any of these daughter phases would have on the

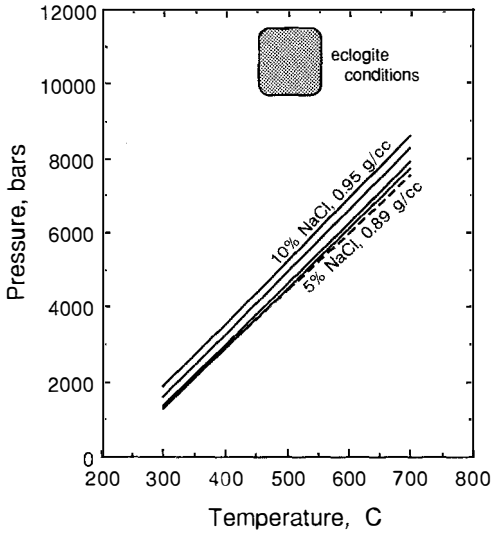

Fig. 9. Model isochores calculated from *type 2* fluid inclusions lacking halite and sylvite daughter minerals in Vi 385. *Solid lines* are for inclusions with model density of 0.95 g cm^3 and 10–14 wt% eq NaCl; *dashed line* is for inclusions with model density of 0.89 g cm^3 and 5 wt% eq NaCl. Model densities assume inclusions are confined to H_2O-NaCl system; all inclusions contain daughter crystals indicating more complex compositions, however. Eclogite *P–T* conditions shown for reference. See text for discussion

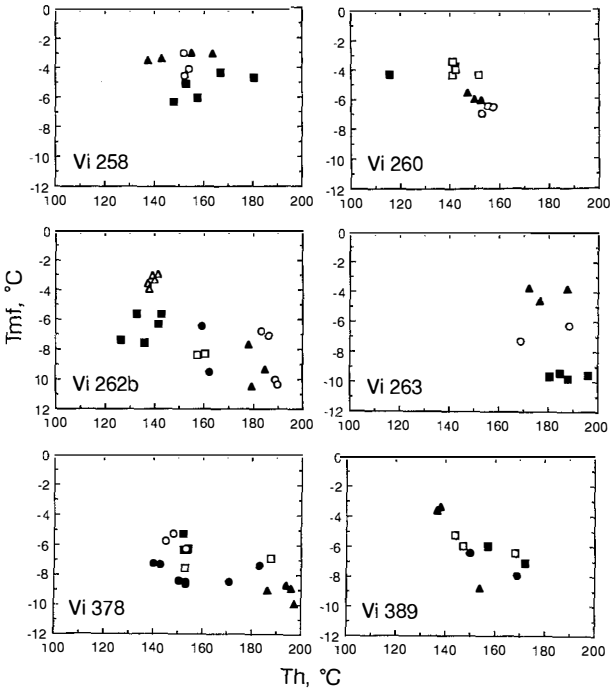

Fig. 10. Temperature of final melting (*T*mf) vs temperature of homogenization (*T*h) diagrams for samples Vi 258, 260, 262b, 263, 378, and 389. In each diagram, the different *symbols* represent clusters of *type 1b* fluid inclusions in different grains. Variations in *T*mf at approximately constant *T*h imply that the recorded 'primary' fluid composition varies from grain to grain. Variations in *T*h at approximately constant *T*mf imply post-entrapment modification of fluid densities (see text)

densities of the inclusions, nor are PVT data available for any of the systems involving these phases. Hence, the pressure underestimate probably represents the combined effects of density modification during uplift and compositional uncertainties arising from the complex daughter mineral suite. As stated above, however, we believe that the strong textural evidence that *type 2* inclusions are primary and were trapped during growth of successive oscillatory zones in the host omphacite allows us to use the inclusion compositions as indicators of fluids present during eclogite vein formation, despite the reset densities.

Fluid heterogeneities

In detail, the pyroxene microthermometric data presented in Figs. 6, 7 show considerable variation. Specifically, *T*mfs range between −12.5 and −2.9 °C and do not display a marked maximum. Within individual samples, *T*mf, *T*h and the daughter mineral assemblage are consistent within individual grains but vary significantly from one grain to another. In Fig. 10, *T*h is plotted versus *T*mf for *type 1b* inclusions in different grains in each of the following samples. Vi 258, 260, 262b, 263, 378 and 389. In each diagram, the different symbols are for different grains. Two types of variations can be recognized: (1) variations of *T*mf at relatively constant *T*h; (2) variations of *T*h at nearly constant *T*mf. Variation of *T*mf at constant *T*h indicates that the composition of the fluid inclusions varies from one grain to another; thus densities must vary also, despite the similar *T*h values. This compositional variation may be either primary or secondary in origin. On the other hand, variations of *T*h at constant *T*mf may reflect variations in the temperature of entrapment of different generations of fluids of constant composition and/or post-entrapment density modification. Significant variations in entrapment *T* would imply variations in the temperature of nucleation of adjacent pyroxene grains, which seems somewhat unlikely. A more probable explanation is that post-entrapment volume changes have selectively modified the densities, and hence these variations are considered to be secondary in origin.

Because microthermometric data were difficult to obtain in *type 2* fluid inclusions, we were unable to determine relative values of *T*mf and *T*h of inclusions lining adjacent bands within the same oscillatory-zoned grain. However, the daughter mineral assemblage documented by microprobe analysis varies dramatically from one fluid inclusion band to another (e.g., Fig. 4), suggesting that fluid composition also varied between adjacent fluid inclusion bands. It is difficult to envision a scenario by which inclusions in adjacent growth zones could have been modified by post-entrapment processes to produce, for example, baddeleyite daughter crystals in one layer, barite in another, and monazite in yet another; hence, we believe that the compositional heterogeneities recorded by *type 2* inclusions are primary in origin.

As shown in Fig. 5, significant compositional differences exist between adjacent oscillatory-zoned pyroxene grains. Location of fluid inclusion bands exclusively

within diopside-rich zones, however, shows that there is a close relationship between the presence of fluid inclusions and the compositional zoning. This suggests that the chemical variations in omphacite may be associated with local variations in fluid composition that are manifested in the crystal-fluid boundary kinetics. This is supported by the occurrence of different daughter minerals between adjacent fluid inclusion bands within the same crystal. The presence of discontinuous fluid inclusion bands parallel to optically continuous growth zones (Figs. 3a, 4) may suggest, moreover, that a free fluid phase was not distributed uniformly along the same growing crystallographic face. A heterogeneous distribution of dislocations acting as sites for fluid entrapment may have accommodated both the development of discontinuous fluid inclusion bands within one growth zone and the random location of inclusion bands between adjacent grains. In any case, the lack of correlation between growth zones of adjacent grains argues against development of the oscillatory zoning in response to changes in temperature, pressure, or degree of supercooling, as are often invoked for oscillatory-zoned pyroxene and plagioclase in magmatic environments (e.g., Loomis and Welber 1982; Smith and Lofgren 1983), or to discrete phases of vein opening; it remains possible that small-scale fluid heterogeneities within individual veins may have partially controlled development of the zonation.

Fluid migration mechanisms

Identical mineral assemblages (i.e., omphacite-garnet-rutile-apatite) are found in both the mylonites and the veins, suggesting that veining is not a response to a particular metamorphic reaction and that the *P–T* conditions remained grossly constant during both foliation development and fracturing. Consequently, devolatilization reactions induced by temperature changes (e.g., Walther and Orville 1982) or thermal expansion of water (e.g., Norris and Henley 1976) can be ruled out as the driving mechanism controlling fracturing and vein formation in the Lago Superiore metagabbros.

Restriction of the veins to highly deformed ductile shear zones, combined with the presence of equivalent mineral assemblages in both the veins and the host mylonites, implies that the fractures formed during ductile deformation at eclogite *P-T* conditions. Similar microthermometric behavior of fluid inclusions in mylonite porphyroclasts and in vein pyroxenes (i.e., *type 1a* and *1b* inclusions) is also consistent with the assumption that synkinematic recrystallization and veining are intimately related.

Yardley (1986) suggested that rocks that deform during metamorphism may undergo reduction in permeability due to extensive synkinematic recrystallization. We believe that dynamic recrystallization of large-strained clasts into a fine-grained mylonitic matrix played a critical role in lowering the permeability of the Monviso rocks by sealing off the pore spaces and thus preventing fluid escape; the resulting increase in pore fluid pressure

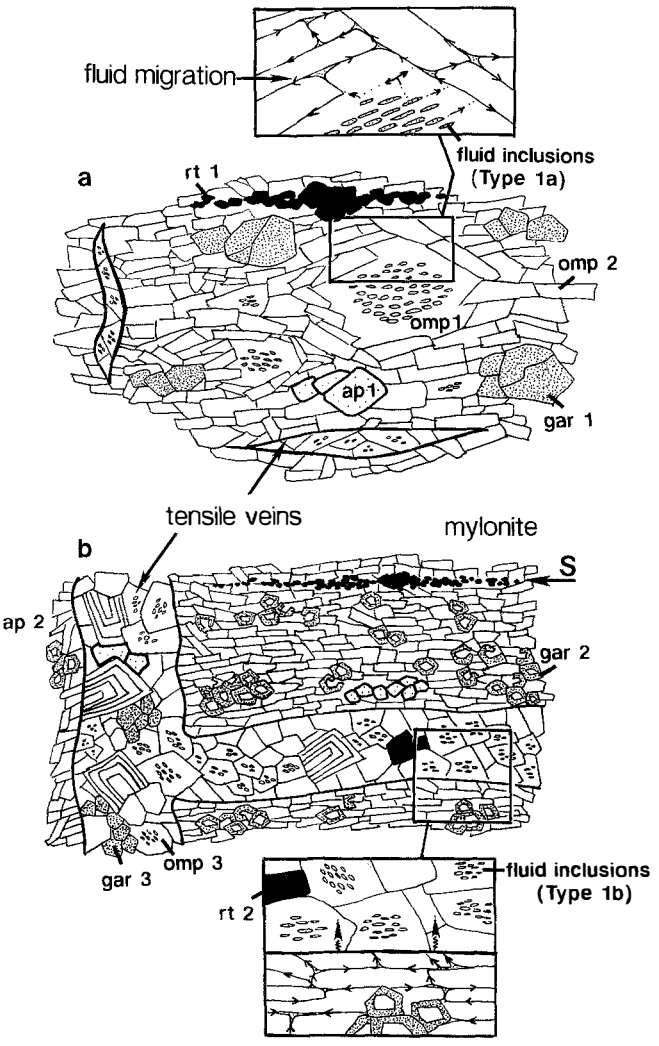

Fig. 11 a, b. Possible model of fluid migration involving localized fluid production and transport during ductile-brittle deformation of the Lago Superiore metagabbros. **a** and **b** are sketches corresponding to two different increments of shear and fluid release, which together with reduction of porosity due to plastic flow lead to cracking (see text for discussion). **a** First increment of cracking in a moderately-strained mylonitic layer. Dynamic recrystallization of fluid inclusion-rich pyroxene clasts releases early inclusion fluids, which in turn promotes dislocation flow and subsequently wets the grain boundaries of the minerals; *omp1* = relic pyroxene clasts; *omp2* = recrystallized pyroxene grains; *gar1, rt 1,* and *ap1* = fragmented garnet, rutile, and apatite. **b** Subsequent development of tensile fractures oriented parallel and normal to the foliation (*S*) and crosscutting what is now a highly-strained mylonitic layer; *gar 2* = atoll-shaped garnets; *omp3* = vein pyroxene (concentric lines in some grains indicate oscillatory growth zones lined with *type 2* fluid inclusions); gar3, *rt2, ap2* = vein garnet, rutile, apatite. *Arrows* point to fluids wetting the grain boundaries of the minerals in the mylonitic rocks and show subsequent migration of the fluids within the veins

led to cracking. Furthermore, because *type 1a* fluid inclusions only occur in preserved porphyroclasts, whereas recrystallized strain-free grains are generally fluid inclusion-free, dynamic recrystallization provides a mechanism to generate a fluid phase internally by release of early inclusion fluids (Fig. 11). This fluid is likely to have enhanced dislocation flow and in turn wet the grain

boundaries of the minerals, thus favoring pressure solution and possibly also promoting crack propagation controlled by stress corrosion (e.g., Anderson and Grew 1977).

Although fragmentation of rutile, garnet and apatite grains and rearrangement of fragments during foliation development (i.e., cataclastic flow) could have counteracted the reduction in porosity due to plastic flow (e.g., Paterson 1978), several features suggest that this effect was minimal: (1) the mylonitic layers contain on average 50–70% omphacite and therefore plastic rather than cataclastic flow was the dominant deformation mechanism; (2) garnet, rutile and apatite are all present in veins, implying that these phases underwent significant dissolution in addition to fragmentation; (3) in highly deformed layers, garnet grains are atoll-shaped and occur as rings surrounding individual recrystallized pyroxenes; these may represent recrystallized garnets that nucleated along the pyroxene grain boundaries in order to reduce the grain surface energy.

In the field, veins occur in both extensional and shear fractures. The presence of *dilatant fractures* parallel to and *tension gashes* normal to the strain markers suggests that both types formed as tensile fractures, requiring that the fluid pressure exceeded the least principal compressive stress by at least the tensile strength of the rock. Because the eclogitic metagabbros are strongly anisotropic, hydraulic fracturing parallel to the foliation plane (i.e., plane of greatest weakness) could have occurred even in the absence of a major deviatoric stress. *Shear fractures* and/or foliation boudinage veins, however, require formation under a deviatoric stress. As pointed out by Yardley (1986), fracturing under a deviatoric stress can occur at $P_{\text{fluid}} < P_{\text{load}}$, sustaining a relatively low rock permeability. Because most veins show complex geometries, it remains difficult to determine the dominant vein types in the field. *Tension gashes* are, however, clearly less abundant than *shear fractures*. Moreover, *shear fractures* and boudinage veins are generally much larger (10 cm–1 m) than the extensional fractures (centimeters). From these, it is suggested that the dominant cause of veining could have been reduction of the bulk-rock permeability during dynamic recrystallization, as a result of which fluid pressure did not necessarily exceed lithostatic pressure.

From the discussion above, it seems reasonable to assume that fracturing occurred when a period of fluid release coincided with ductile deformation. Recognition of a crack-seal vein geometry in some *tension gashes* (Philippot 1987) further suggests that pulses of fluid release rather than a steady flow of fluid-controlled mineral deposition and growth in veins. Ductile deformation probably occurred discontinuously by successive increments of shearing that resulted in periodic cycles of pore pressure increase, brittle failure, subsequent migration of fluid towards the veins and associated drop in fluid pressure. In this model, the rate of fluid release and the reduction in porosity that together lead to cracking depend on the rate of plastic flow. Therefore, small-scale fluid equilibrium in veins (recorded by *type 2* inclusions) is best interpreted in terms of a diffusion mechanism controlling localized heterogeneous fluid production and transport rather than relatively rapid pervasive flow along grain boundaries and/or discrete microcracks; this model is summarized in Fig. 11.

The occurrence of meter-scale *shear fractures,* however, also points to a second mechanism of fluid transport involving a large influx of fluids, perhaps derived from hydrous layers associated with the metagabbros, into spaced cracks. As discussed above, large shear fractures may have formed at $P_{\text{fluid}} < P_{\text{load}}$. If this were true, the permeability of the rocks may have remained relatively low during shear failure and fluid flow was limited. The different types of vein structures may represent a continuous variation in the scale of fluid mobility from heterogeneous diffusion-controlled fluid flow in small tension gashes and dilatant fractures to channelled fluid flow into large shear fractures (see Yardley 1983).

It is not yet clear if the fluid heterogeneities recorded by *type 2±1b* fluid inclusions in the veins correspond to separate pulses of fluid associated in time with distinct increments of shear, or rather a single pulse of several contemporaneous packets of fluid with different composition. In the crack-seal type of veins, we were unable to determine any marked fluid composition variations between *type 3* inclusions in adjacent healed microcracks, thus precluding demonstration that successive crack increments were followed by the sealing in of brines of specific composition. In oscillatory-zoned pyroxene, however, the lack of correlation of fluid inclusion bands between adjacent grains argues against discrete increments of shear and fluid release controlling periodic episodes of vein infilling and suggests that local fluid-composition gradients indeed may have existed at a single instant in time.

Discussion and conclusions

Recently, Sorensen and Barton (1987) and Sorensen (1988) have suggested that large-scale, subduction-related metasomatism induced amphibolitization of eclogitic blocks and melting at $P \sim 8$–11 kbar and $T \sim 640$–750 °C in the Catalina Schist, southern California. In the same region, Bebout and Barton (1989) documented large-scale fluid flow and mass transfer at 25–45 km depth during subduction zone metamorphism. In contrast, Franz et al. (1989) and Selverstone et al. (1990) present evidence from eclogitic veins in interlayered mafic rocks and tuffaceous material from the Tauern Window (Eastern Alps) that argues for localized fluid segregation rather than pervasive fluid flow at 60–70 km depth during subduction. Their results suggest that extensive fluid flow may be inefficient at depth during H*P*-L*T* metamorphism and that fluids (i.e. in contrast to melts?) thus may play only a local role in metasomatic transfer of material from the downgoing slab to the mantle wedge. The preservation of apparent small-scale fluid heterogeneities in the Monviso eclogites suggests limited fluid transport at this locality as well. Although more detailed study of vein systems is needed to further constrain the scales and mechanisms controlling metasomatic pro-

cesses in H*P*-L*T* terranes, the existing data argue for a variety of fluid transport mechanisms operating at different scales and at different pressures.

The daughter mineral suite in the Monviso samples indicates high solubilities of Na, K, Ca, Mg, Fe, Si, Al, Zr, Ti, P, Ba, Ce, La, Th, and S in aqueous brines at a minimum pressure of 10–11 kbar. The presence of monazite, rutile, and sphene daughter minerals is in general agreement with studies indicating that REE solubilities increase with increasing chloride molalities in aqueous brines (e.g., Flynn and Burnham 1978) and that TiO_2 solubility increases with both pressure (Ayers and Watson 1989) and salinity (J.M. Brenan, personal communication). In contrast to the conclusions of Cann (1970), Pearce and Norry (1979) and Tatsumi et al. (1986), it appears from the daughter mineral suite that high-field strength elements (HFSE) can be present in significant amounts in aqueous brines, at least at moderately H*P*-L*T* conditions, and hence could be transported as dissolved species. This is consistent with Sorensen and Grossman's (1989) study of garnet-amphibolite blocks in an ultramafic melange in the Catalina Schist, showing that fluid infiltration at 30–40 km depth caused REE, HFSE, Sr, Th and U metasomatism. As noted above, however, our results suggest only limited transport of the trace-element-rich fluids at Monviso.

Documenting the mobility of trace elements in subduction zones is of critical importance to our understanding of island-arc magma genesis and element recycling to the mantle wedge. One of the major criteria used to distinguish island-arc basalts from N-type MORB (e.g., Hawkesworth and Powell 1980; Perfit et al. 1980; Arculus and Powell 1986; Vidal et al. 1989) is the relative enrichment of low-ionic potential elements (K, Ba, Sr, Rb) and low abundances of elements of high-ionic potential (Zr, Ti, P, Ce, Ta, Nd, HF, Sm, Yb, Y, Sc, Cr) in the island-arc basalts. Based on the assumption that low-ionic potential elements are easily mobilized by a fluid phase, their enrichment in island-arc basalts has been attributed to selective metasomatism of their mantle source region by fluid derived from the subducted slab (e.g., Ryerson and Watson 1987; Wilson 1989). The results of this study, however, argue against such selective metasomatism: the Monviso samples provide clear evidence that high-field-strength elements, as well as large-ion-lithophile and light-REE, can be present in saline brines at depth, implying that they also could be recycled to the mantle wedge in substantial abundances if the fluids can be removed from the downgoing slab. This would be consistent with the observed enrichment of Zr, Ti, Fe, Al, Ca, LREE, Ba, K, Sr, Cl, P and H_2O in metasomatized mantle xenoliths (e.g., Harte 1987; Lloyd et al. 1987). In the case of the Monviso samples, however, the fluids do not appear to have been transported any great distance during subduction to $\sim$40 km depth. We conclude that fluid transport mechanisms are as important in controlling metasomatism of the mantle wedge as are the relative solubilities of the various indicator trace elements. Clearly, however, more detailed studies of fluid transport mechanisms at high pressures are needed to document more fully the relationships between subduction zone metamorphism, mantle metasomatism, and magma generation.

Acknowledgments. We thank Sorena Sorensen, Virginia Sisson, Harvey Belkin and John Ferry for their very thoughtful reviews of the manuscript, C.J. Knight of the Virginia Polytechnic Institute and State University for her patience and assistance with the Raman analyses, and X. Barrientos for discussion. Funding for this research was provided by NSF grants EAR 86-58145 and EAR 88-17152 to Selverstone.

References

Andersen T, Burke EAJ, Austrheim H (1989) Nitrogen-bearing, aqueous fluid inclusions in some eclogites from Western Gneiss Region of the Norwegian Caledonides. Contrib Mineral Petrol 103:153–165

Anderson OL, Grew PC (1977) Stress corrosion theory of crack propagation with applications to geophysics. Rev Geophys Space Phys 15:77–104

Arculus RJ, Powell R (1986) Source of component mixing in the regions of arc magma generation. J Geophys Res 91:5913–5926

Ayers JC, Watson EB (1989) Solubility of accessory minerals in H_2O at upper mantle conditions (abstract). EOS 70:506

Bebout GE, Barton MD (1989) Fluid flow and metasomatism in a subduction zone hydrothermal system: Catalina schist terrane, California. Geology 17:976–980

Bodnar RJ (1982) Fluid inclusions in porphyry-type deposits. Course notes, Miner Deposits Res Rev Ind, P State Univ

Cann JR (1970) Rb, Sr, Y, Zr and Nb in some ocean floor basaltic rocks. Earth Planet Sci Lett 10:7–11

Crawford ML (1981) Phase equilibria in aqueous fluid inclusions. In: Hollister LS and Crawford ML (eds) Fluid Inclusions: Applications to Petrology. Mineral Assoc Can Short Course: 75–100

Dal Piaz GV (1974) Le métamorphisme alpin de haute pression et basse température dans l'évolution structurale du bassin ophiolitique Alpino-Apennique. Bull Soc Geol Ital 11:433–446

Elter G (1971) Schistes lustrés et ophiolites de la zone piémontaise entre Orco et Doiré Baltée (Alpes Graies). Géol Alp 47:147–169

Ernst WG (1972) CO_2-poor composition of the fluid attending Franciscan and Sanbagawa low-grade metamorphism. Geochim Cosmochim Acta 36:497–504

Ernst WG, Dal Piaz GV (1978) Mineral parageneses of eclogitic rocks and related mafic schists of the piemonte ophiolite nappe, Breuil St-Jacques area, Italian Western Alps. Am Mineral 63:621–640

Flynn RT, Burnham CW (1978) An experimental determination of rare earth partition coefficients between a chloride containing vapor phase and silicate melts. Geochim Cosmochim Acta 42:684–702

Franz G, Thomas S, Selverstone J (1989) Fluid in eclogites: Evidence from high-pressure veins in the Australian Alps (abstract). EOS 70, 43:1377

Haasen P, Lawson AW (1958) Der Einfluß hydrostatischen Druckes auf die Zugverformung von Einkristallen. Z Metallkd 49:280–291

Harte B (1987) Metasomatic events recorded in mantle xenoliths: an overview. In: Nixon PH (ed) Mantle xenoliths. John Wiley and Sons, New York, pp 625–640

Hawkesworth CJ, Powell M (1980) Magma genesis in the Lesser Antilles island arc. Earth Planet Sci Lett 51:297–308

Holland TJB (1979) High-water activities in the generation of high pressure kyanite eclogites of the Tauern Window, Austria. J Geol 87:1–27

Kienast JR (1983) Le métamorphisme de haute pression et basse temperature (éclogites et schistes bleus): données nouvelles sur la pétrologie des roches de la croûte océanique subductée et des sédiments associés. Thèse de doctorat d'Etat, Univ. Paris VI

Klemd R (1989) PT evolution and fluid inclusion characteristics of retrograded eclogites, Münchberg gneiss complex, Germany. Contrib Mineral Petrol 102:221–229

Lardeaux JM, Caron JM, Nisio P, Péquignot G, Boudeulle M (1986) Microstructural criteria for reliable thermometry in low-temperature eclogite. Lithos 19:187–203

Lloyd FE, Nixon PH, Hornung G, Condliffe E (1987) Regional K-metasomatism in the mantle beneath the west branch of the east African rift: alkali clinopyroxenite xenoliths in highly potassic magmas. In: Nixon PH (ed) Mantle xenoliths. John Wiley and Sons, New York, pp 655–659

Lombardo B, Nervo R, Compagnoni R, Messiga B, Kienast JR, Mevel C, Fiora L, Piccardo GB, Lanza R (1978) Osservazioni preliminari sulle ofiolite metamorfiche del Monviso (Alpi Occidentali). Rend Soc Ital Mineral Petrol 34:253–305

Loomis TP, Welber PW (1982) Crystallization processes in the Rocky Hill Granodiorite Pluton, California: An interpretation based on compositional zoning of plagioclase. Contrib Mineral Petrol 81:230–239

Luckscheiter B, Morteani G (1980) Microthermometrical and chemical studies of fluid inclusions from Alpine veins from the penninic rocks of the central and western Tauern Window, Austria, Italy. Lithos 13:61–77

Matthews A, Schliestedt M (1984) Evolution of the blueschist and greenschist facies rocks of Sifnos, Cyclades, Greece: a stable isotope study of subduction-related metamorphism. Contrib Mineral Petrol 88:150–163

Norris RJ, Henley RW (1976) Dewatering of a metamorphic pile. Geology 4:333–336

Paterson MS (1978) Experimental rock deformation, the brittle field. In: Wyllie PJ (ed) Mineral and rocks, vol 13. Springer, Berlin Heidelberg New York

Peacock SM (1990) Fluid processes in subduction zones. Science 248:329–337

Pearce JA, Norry MJ (1979) Petrogenetic implications of Ti, Zr, Y and Nb variations in volcanic rocks. Contrib Mineral Petrol 69:33–47

Perfit MR, Gust DA, Bence AE, Arculus RJ, Taylor SR (1980) Chemical characteristics of island-arc basalts: implications for mantle sources. Chem Geol 30:227–256

Philippot P (1987) «Crack seal» vein geometry in eclogitic rocks. Geodinamica Acta 1, 3:171–181

Philippot P (1988) Déformation et éclogitisation progressives d'une croûte océanique subductée: l'exemple du Monviso, Alpes occidentales. Contraintes cinématiques durant la collision alpine. Documents et Travaux du Centre Géologique et Géophysique de Montpellier, France

Philippot P, Kienast JR (1989) Chemical-microstructural changes in eclogitic shear zones, Monviso (Western Alps), as indicators of strain history, mechanisms and scales of mass transfer. Lithos 23:179–200

Platt JP, Vissers RLM (1980) Extensional structures in anisotropic rocks. J Struct Geol 2:397–410

Roedder E (1984) Fluid inclusions. In: Ribbe PH (ed) Reviews in Mineralogy 12 Mineral Soc Am Washington DC

Ryerson FJ, Watson EB (1987) Rutile saturation in magmas: implications for Ti-Nb-Ta depletion in island-arc basalts. Earth Planet Sci Lett 86:225–239

Selverstone J (1986) Possible consequence of CO_2-H_2O immiscibility on blueschist-facies metamorphism (abstract). Geol Soc Am Abstracts Program 18:745

Selverstone J, Franz G, Thomas S (1990) Fluids at high pressure: inferences from 20 kbar eclogites and associated veins in the Tauern Window, Austria (abstract). Goldschmidt Conference, Baltimore

Smith RK, Lofgren GE (1983) An analytical and experimental study of zoning in plagioclase. Lithos 16:153–168

Sobolev NV, Dobretsov NL, Bakirov AB, Shatski VS (1986) Eclogites from various types of metamorphic complexes in the USSR and the problems of their origin. In: Evans BW, Brown EH (eds) Blueschists and eclogites. Geol Soc Am Mem 164, pp 313–332

Sorensen SS (1988) Petrology of amphibolite-facies mafic and ultramafic rocks from the Catalina schist, southern Catalina: metasomatism and migmatization in a subduction metamorphic setting. J Metamorphic Geol 6:405–435

Sorensen SS, Barton MD (1987) Metasomatism and partial melting in a subduction complex: Catalina schist, southern California. Geology 15:115–118

Sorensen SS, Grossman JN (1989) Enrichment of trace elements in garnet amphibolites from a paleo-subduction zone: Catalina schist, southern California, Geochim Cosmochim Acta 53:3155–3177

Sterner SM, Bodnar RJ (1989) Synthetic fluid inclusions-VII. Re-equilibration of fluid inclusions in quartz during laboratory-simulated metamorphic burial and uplift. J Metamorphic Geol 7:243–360

Tatsumi Y, Hamilton DL, Nesbitt RW (1986) Chemical characteristics of fluid phase released from a subducted lithosphere and origin of arc magmas: evidence from high-pressure experiments and natural rocks. J Volcanol Geothermal Res 29:293–309

Taylor HP, Coleman RG (1968) O18/O16 ratios of coexisting minerals in glaucophane-bearing metamorphic rocks. Geol Soc Am Bull 79:1727–1756

Vidal P, Dupuy C, Maury R, Richard M (1989) Mantle metasomatism above subduction zones: Trace-element and radiogenic isotope characteristics of peridotite xenoliths from Batan Island (Philippines). Geology 17:1115–1118

Walther JV, Orville PM (1982) Volatile production and transport in regional metamorphism. Contrib Mineral Petrol 79:252–257

Watson EB, Brenan JM (1987) Fluids in the lithosphere, 1. Experimentally determined wetting characteristics of CO_2-H_2O fluids and their implications for fluid transport, host-rock physical properties, and fluid inclusion formation. Earth Planet Sci Lett 85:497–515

Williams-Jones AE, Samson IM (1990) Theoretical estimation of halite solubility in the system NaCl-$CaCl_2$-H_2O: applications to fluid inclusions. Can Mineral 28:299–304

Wilson M (1989) Igneous petrogenesis, a global tectonic approach. Unwin Hyman, London Boston Sydney Wellington

Wyllie PJ (1984) Constraints imposed by experimental petrology on possible and impossible magma sources and products. Philos Trans R Soc London A310:439–456

Wyllie PJ (1988) Magma genesis, plate tectonics, and chemical differentiation of the earth. Rev Geophys 26:370–404

Yardley BWD (1983) Quartz veins and devolatilization during metamorphism. J Geol Soc London 140:657–663

Yardley BWD (1986) Fluid migration and veining in the Connemara schists. Ireland. In: Walther JV, Wood BJ (eds) Fluid-rock interactions during metamorphism. (Advances in physical geochemistry, vol 5) Springer-Verlag, pp 109–131

Yardley BWD, Bottrell SH (1988) Immiscible fluids in metamorphism: implications of two-phase flow for reaction history. Geology 16:199–202

Zhang Y, Frantz JD (1987) Determination of the homogenization temperatures and densities of supercritical fluids in the system $NaCl-KCL-CaCl_2-H_2O$ using synthetic fluid inclusions. Chem Geol 64:335–350